Contents lists available at ScienceDirect

Mechanical Systems and Signal Processing

A fully-coupled dynamic model for the fundamental shear horizontal wave generation in a PZT activated SHM system

Peng Li [a,b], Shengbo Shan [a], Fuzhen Wen [a], Li Cheng [a,*]

[a] Department of Mechanical Engineering, The Hong Kong Polytechnic University, Hong Kong, PR China
[b] School of Human Settlements and Civil Engineering, Xi'an Jiaotong University, Xi'an 710049, PR China

ARTICLE INFO

ABSTRACT

The fundamental shear horizontal (SH0) wave in plate-like structures is of great importance in structural health monitoring (SHM) applications due to its unique non-dispersive nature. Its generation or reception using piezoelectric (PZT) wafers, however, is always a critical and challenging issue. In this study, a theoretical model on the shear horizontal (SH) wave generation is established based on the continuum mechanics theory. The model considers the dynamic properties of a PZT actuator and its coupling with a host plate through a bonding layer, whose mechanical property is modelled by considering a continuous shear stress but different tangential displacements across the adhesive layer. Closed form solutions are obtained using the trigonometric series decomposition and the modal superposition method. The solution series are shown to exhibit fast convergence. The model, along with some typical physical phenomena, is validated through comparisons with the FEM and experimental results. Numerical analyses allow establishing a series truncation criterion, in relation to the size of the actuator and the wavelength of the SH0 wave. It is shown that the dynamic coupling between the PZT and the plate should be considered in the design of PZT-activated SH0 wave generation. Typical phenomena in different frequency regions and their impact on the SH0 wave generation are scrutinized and discussed. The proposed theoretical model is expected to provide a useful tool for the physical mechanism exploration, structural design and eventually system optimization for SH0 wave generation in SHM applications.

© 2018 Elsevier Ltd. All rights reserved.

1. Introduction

The ultrasonic inspection based on guided waves, a combination of the wave emission and the ultrasonic characterization, has shown its effectiveness for structural damage detection and has been extensively applied in non-destructive evaluations (NDE) and the structural health monitoring (SHM) [1–4]. Conventional guided waves include Lamb waves with symmetric and anti-symmetric modes and shear horizontal (SH) waves in plates. Among numerous techniques employed in the SHM, Lamb waves have been intensively explored, owing to their unique features such as strong penetration, long-distance transmission, omnidirectional dissemination and high sensitivity to damage etc. [3–6]. However, Lamb waves are dispersive in nature, with frequency-dependent phase and the group velocities. Waves are therefore distorted during propagation, which increases the complexities for the signal processing, especially when the wave packet interacts with cracks and/or defects. Compared with Lamb waves, one of the most appealing advantages of the fundamental shear horizontal (SH0) waves is its

---

non-dispersive property. Therefore, the shape of the wave packet remains unchanged during the propagation, thus facilitating the interpretation of the received signals to some extent [7–8]. Moreover, the SH0 waves do not involve out of-plane particle displacements. The wave propagation is then less prone to the surrounding media, which is also attractive for SHM applications [9]. Hence, SH0 wave-based techniques show great potential in SHM applications.

The successful SH0 wave generation and a thorough understanding of the underlying physical mechanism are the prerequisite for the implementation of SH0 wave-based SHM techniques. Well-known methods include magnetostrictive transducers [10], electromagnetic acoustic transducers (EMAT) [11], interdigital PVDF [12,13] and shear horizontal piezoelectric wafer active sensor (SH-PWAS) [8,14]. Studies have been carried out to ensure the effective SH0 wave generation. Among these techniques, SH-PWAS is a popular choice, shown to be efficient and also cost-effective for SH0 wave generation in plates, with the piezoelectric transducers working in different modes, such as d_{15} [9], d_{35} [8], d_{24} [15–16] and d_{36} [7,17,18] modes. Specifically, for the d_{15} mode, with the poling direction of the piezoelectric wafer parallel to the surface of the plate and the electric field on the thickness direction, SH waves (including SH0 wave) can be generated and propagate along the direction perpendicular to the poling direction. For instance, a flexible d_{15} PZT transducer is used to generate SH0 waves with directionality in the low frequency range of 20–120 kHz [19]. Besides, to predict the directivity patterns of contact type ultrasonic transducers in the generation of guided waves, a novel 2D analytical model based on the Huygens's principle is proposed by Tiwari et al. [20], in which affiliated SH0 wave with 80 kHz is obtained through finite element modeling and verified by experiments. Recently, SH0 wave generation and reception using a synthesized face-shear deformation mode in a thickness-poled piezoelectric wafer have also been investigated [21].

Despite the vast FEM-based numerical investigations and experimental attempts on the SH wave excitation, there is still a lack of general theoretical method/model to systematically describe the generation process of the SH waves, which is the motivation and the contribution targeted by this paper. Such a model would allow revealing the mechanism of the SH wave generation on one hand, and providing guidance to the design of the SH-wave-based SHM system configurations in terms of the actuator size and excitation patterns to achieve the desired system performance on the other hand. Motivated by this, this work is dedicated to the development of such a theoretical model for further SHM applications.

In this paper, a theoretical model for the SH0 wave generation using d_{15} mode piezoelectric transducers is established based on the continuum mechanics theory, in which the transducer is bonded on a plate through an adhesive layer. Upon exciting the PZT actuator with an input voltage, SH waves are generated in the plate through the bonding layer. In the process, the dynamics of the PZT intervene and are coupled with the system, which is referred to as "dynamic coupling" in the following discussions. In the proposed model, the bonding layer between the PZT actuator and the plate is simulated through its thickness and shear modulus, instead of solving complex governing dynamic equations [22–24]. Analytical solutions, expressed in the form of trigonometric series, are then obtained, which can simultaneously satisfy the governing dynamic equations and the boundary conditions of the coupled PZT-plate system. The convergence of the series is first assessed, following by a comprehensive FEM validation process in both time and frequency domains. Additionally, experiments are carried out for further model validations and phenomenon verifications. After that, influences of the dynamic coupling on the system performance under different bonding conditions in different frequency ranges are investigated in detail to better understand the underlying physics and the impact on SHM system design.

2. Theoretical model

The two-dimensional model under investigation is composed of a PZT wafer (d_{15} mode), with a length $2a$, bonded on the surface of an infinite metal plate through a thin bonding layer, as shown in Fig. 1. The thickness of the PZT and the plate are denoted by h^p and h_s, respectively. The upper PZT belongs to transversely isotropic piezoelectric materials poled along the positive z direction which is determined from x and y by the right-hand rule and is assumed to be infinite in this model. The bonding layer, with parameters equivalent to an adhesive thickness typically in the range of 1–100 μm [25], is taken into account.

2.1. Governing equations

Driven by an alternating voltage imposed on the surfaces of the PZT, SH waves can be excited and propagate along ± x directions in the plate. Under the framework of the continuum mechanics theory, the displacement vector $\boldsymbol{u}$ and electric potential function φ in the PZT can be expressed as [26,27]
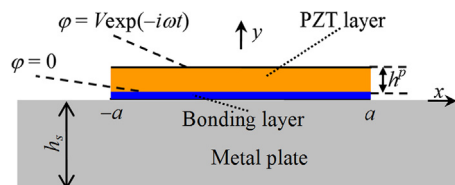

Fig. 1. Theoretical model.

$$u_1 = u_2 = 0, u_3 = u(x, y, t), \varphi = \varphi(x, y, t). \tag{1}$$

Using the linear piezoelectricity theory, the corresponding stresses (σ_{zx} and σ_{zy}) and electric displacements (D_x and D_y) in the PZT actuator write

$$\begin{cases} \sigma_{zx} = c_{44} \frac{\partial u}{\partial x} + e_{15} \frac{\partial \varphi}{\partial x}, \ \sigma_{zy} = c_{44} \frac{\partial u}{\partial y} + e_{15} \frac{\partial \varphi}{\partial y}, \\ D_x = e_{15} \frac{\partial u}{\partial x} - \varepsilon_{11} \frac{\partial \varphi}{\partial x}, \ D_y = e_{15} \frac{\partial u}{\partial y} - \varepsilon_{11} \frac{\partial \varphi}{\partial y}. \end{cases} \tag{2}$$

where c_{44}, e_{15} and ε_{11} are the elastic, piezoelectric and dielectric constants, respectively. Hence, the dynamic equations governing the PZT layer can be written as

$$c_{44}\nabla^2 u + e_{15}\nabla^2 \varphi = \rho^p \frac{\partial^2 u}{\partial t^2}, e_{15}\nabla^2 u - \varepsilon_{11}\nabla^2 \varphi = 0. \tag{3}$$

where ρ^p is the mass density, ∇^2 is the two-dimensional (2D) Laplacian, and t is the time. Similarly, the stress component σ_{zy} in the plate can be obtained by $\sigma_{zy} = \mu^s \frac{\partial u}{\partial y}$ with μ^s being the shear modulus. Hence, the governing dynamic equation for the plate is given by

$$\mu^s \nabla^2 u = \rho^s \frac{\partial^2 u}{\partial t^2}, \tag{4}$$

with ρ^s being the mass density of the plate.

2.2. Boundary conditions

The PZT layer is traction free and electricity open-circuited at $x = \pm a$, which requires

$$x = \pm a : D_x = 0, \sigma_{zx} = 0 \quad \text{for} \quad 0 < y < h^p. \tag{5}$$

With the PZT acting as an actuator, a harmonic driving voltage $V\exp(-i\omega t)$ is imposed on the piezoelectric strip, leading to the following boundary conditions:

$$y = h^p : \varphi = V \exp(-i\omega t), \sigma_{zy} = 0 \quad \text{for} \quad |x| \leqslant a. \tag{6a}$$

$$y = 0 : \varphi = 0 \quad \text{for} \quad |x| \leqslant a. \tag{6b}$$

Due to its sub-wavelength thickness scale of the bonding layer, i.e., the thickness h is much smaller than the wavelength concerned, the corresponding shear strain can be approximated by $\frac{1}{h}[u(y = h) - u(y = 0)]$. For the same reason, the shear stress is assumed to be identical across the thickness of the bonding layer. Therefore, the stress boundary conditions at the PZT-plate interface can be mathematically written as:

$$\sigma_{zy}(y = 0^-) = \begin{cases} \sigma_{zy}(y = 0^+) = \frac{\mu}{h}[u(y = 0^+) - u(y = 0^-)], \ |x| \leqslant a. \\ 0, \ |x| > a. \end{cases} \tag{6c}$$

where μ stands for the shear modulus of the bonding layer. In this model, both μ and h are adopted to simulate the mechanical property of the bonding layer. While the shear stress is continuous across the adhesive layer, the tangential displacements undergo a jump. As an extreme case, Eq. (6) can be reduced an ideal bonding when u and h approaches to infinity and zero, respectively. Then both displacement and shear stress are continuous.

Besides, the bottom surface of the plate is traction free, which requires

$$y = -h_s : \sigma_{zy} = 0. \tag{6d}$$

In the following, we will focus on finding a theoretical or analytical solution which can satisfy both the governing equations, Eqs. (3) and (4), and the boundary conditions, Eqs. (5) and (6), simultaneously.

2.3. Analytical solutions

The solution of Eq. (3) can be obtained by virtue of the trigonometric function expansion technique [28]. The displacement and the electrical potential function are expressed as follows (hereafter, $\exp(-i\omega t)$ is omitted for brevity):

$$u = [A_0 \cos(\xi_0 y) + B_0 \sin(\xi_0 y)] + \sum_{m=1}^{\infty} [A_m \cos(\xi_m y) + B_m \sin(\xi_m y)] \cos(\alpha_m x), \tag{7a}$$

$$\varphi = \frac{e_{15}}{\varepsilon_{11}}[A_0 \cos(\xi_0 y) + B_0 \sin(\xi_0 y)] + [C_0 y + D_0]$$
$$+ \sum_{m=1}^{\infty} \left\{ \frac{e_{15}}{\varepsilon_{11}}[A_m \cos(\xi_m y) + B_m \sin(\xi_m y)] + [C_m \cosh(\alpha_m y) + D_m \sinh(\alpha_m y)] \right\} \cos(\alpha_m x), \tag{7b}$$

where the undetermined coefficients A_0, B_0, C_0, D_0, A_m, B_m, C_m and D_m will be determined by the boundary conditions mentioned above. In the above expressions, $\alpha_m = \frac{m\pi}{a}$ is the wave number in x direction. The above expressions involve the modal superposition of different mode number m. The wave number ξ_m in y direction can be obtained as $\xi_m = \sqrt{\frac{\omega^2}{\bar{c}_{44}/\rho^p} - \alpha_m^2}$ if the solution in Eq. (7) satisfies dynamic governing equation of the PZT, Eq. (3), with the equivalent shear modulus $\bar{c}_{44} = c_{44} + \frac{e_{15}^2}{\varepsilon_{11}}$. Note that the traction free and electricity open-circuited boundary conditions at $x = \pm a$, i.e., Eq. (5), have been automatically satisfied. Correspondingly, the shear stress component σ_{zy}, which will be used in subsequent boundary conditions, is given by

$$\sigma_{zy} = \bar{c}_{44}\xi_0[-A_0 \sin(\xi_0 y) + B_0 \cos(\xi_0 y)] + e_{15}C_0 + \sum_{m=1}^{\infty} \{\bar{c}_{44}\xi_m[-A_m \sin(\xi_m y) + B_m \cos(\xi_m y)] + e_{15}\alpha_m[C_m \sinh(\alpha_m y)$$
$$+ D_m \cosh(\alpha_m y)]\} \cos(\alpha_m x). \tag{8}$$

For the SH waves in the plate, its displacement can be expressed in terms of the Fourier integral as [29]

$$u = \int_{-\infty}^{\infty} [A_s \cos(\xi_s y) + B_s \sin(\xi_s y)] \exp(iqx) dq, \tag{9}$$

where A_s and B_s are the coefficients to be determined. This expression satisfies the governing equation of the plate, Eq. (4), if $\xi_s = \sqrt{\frac{\omega^2}{\mu^s/\rho^s} - q^2}$. Hence, the corresponding stress component can be obtained as:

$$\sigma_{zy} = \int_{-\infty}^{\infty} \mu^s \xi_s[-A_s \sin(\xi_s y) + B_s \cos(\xi_s y)] \exp(iqx) dq. \tag{10}$$

Substituting Eqs. (7)–(10) into the boundary conditions, Eq. (6), yields the following linear homogeneous equations:

$$\bar{c}_{44}\xi_0[-A_0 \sin(\xi_0 h^p) + B_0 \cos(\xi_0 h^p)] + e_{15}C_0 + \sum_{m=1}^{\infty} \{\bar{c}_{44}\xi_m[-A_m \sin(\xi_m h^p) + B_m \cos(\xi_m h^p)]$$
$$+ e_{15}\alpha_m[C_m \sinh(\alpha_m h^p) + D_m \cosh(\alpha_m h^p)]\} \cos(\alpha_m x) = 0. \tag{11}$$

$$\frac{e_{15}}{\varepsilon_{11}}[A_0 \cos(\xi_0 h^p) + B_0 \sin(\xi_0 h^p)] + [C_0 h^p + D_0]$$
$$+ \sum_{m=1}^{\infty} \left\{ \frac{e_{15}}{\varepsilon_{11}}[A_m \cos(\xi_m h^p) + B_m \sin(\xi_m h^p)] + [C_m \cosh(\alpha_m h^p) + D_m \sinh(\alpha_m h^p)] \right\} \cos(\alpha_m x) = V. \tag{12}$$

$$\frac{e_{15}}{\varepsilon_{11}}A_0 + D_0 + \sum_{m=1}^{\infty} \left(\frac{e_{15}}{\varepsilon_{11}}A_m + C_m \right) \cos(\alpha_m x) = 0. \tag{13}$$

$$\int_{-\infty}^{\infty} -\mu^s \xi_s \tan(\xi_s h_s) A_s \exp(iqx) dq = \frac{\mu}{h} \left[A_0 + \sum_{m=1}^{\infty} A_m \cos(\alpha_m x) - \int_{-\infty}^{\infty} A_s \exp(iqx) dq \right], \ |x| \leqslant a. \tag{14}$$

$$\int_{-\infty}^{\infty} -\mu^s \xi_s \tan(\xi_s h_s) A_s \exp(iqx) dq = \begin{cases} 0, \ |x| > a. \\ (\bar{c}_{44}\xi_0 B_0 + e_{15}C_0) + \sum_{m=1}^{\infty} (\bar{c}_{44}\xi_m B_m + e_{15}\alpha_m D_m) \cos(\alpha_m x), \ |x| \leqslant a. \end{cases} \tag{15}$$

It is noted that the undetermined coefficient A_s can be obtained by inverting the Fourier transform in Eq. (15), giving

$$A_s = -\frac{1}{\mu^s \xi_s \tan(\xi_s h_s)} \left\{ (\bar{c}_{44}\xi_0 B_0 + e_{15}C_0) \frac{\sin(qa)}{\pi q} + \sum_{m=1}^{\infty} (\bar{c}_{44}\xi_m B_m + e_{15}\alpha_m D_m) \frac{(-1)^m q \sin(qa)}{\pi(q^2 - \alpha_m^2)} \right\}. \tag{16}$$

when $\xi_s \tan(\xi_s h_s) = 0$, the phase velocity of the SH waves in the plate with its both the upper and bottom surfaces free can be obtained as:

$$c_{SH} = \sqrt{\frac{\mu^s}{\rho^s}} \sqrt{\left(\frac{m\pi}{qh_s} \right)^2 + 1}, \ (m = 0, 1, 2, \cdots). \tag{17}$$

when $m = 0$ for SH0 wave, $c_{SH0} = \sqrt{\mu^s/\rho^s}$. This velocity only depends on the material parameters of the plate and is frequency-independent and therefore non-dispersive. Multiplying Eqs. (11)–(14) by $\cos(\alpha_n x_3)$ for $n = 0, 1, 2, \ldots$ (with $\alpha_0 = 0$), integrating the resulting equations from $-a$ to a, and substituting Eq. (16) for A_s, the following linear equations in terms of the whole set of the undetermined constants can be obtained:

$$\bar{c}_{44}\xi_0[-A_0\sin(\xi_0 h^p) + B_0\cos(\xi_0 h^p)] + e_{15}C_0 = 0. \tag{18a}$$

$$\bar{c}_{44}\xi_m[-A_m\sin(\xi_m h^p) + B_m\cos(\xi_m h^p)] + e_{15}\alpha_m[C_m\sinh(\alpha_m h^p) + D_m\cosh(\alpha_m h^p)] = 0. \tag{18b}$$

$$\frac{e_{15}}{\varepsilon_{11}}[A_0\cos(\xi_0 h^p) + B_0\sin(\xi_0 h^p)] + [C_0 h^p + D_0] = V. \tag{18c}$$

$$\frac{e_{15}}{\varepsilon_{11}}[A_m\cos(\xi_m h^p) + B_m\sin(\xi_m h^p)] + [C_m\cosh(\alpha_m h^p) + D_m\sinh(\alpha_m h^p)] = 0. \tag{18d}$$

$$\frac{e_{15}}{\varepsilon_{11}}A_0 + D_0 = 0. \tag{18e}$$

$$\frac{e_{15}}{\varepsilon_{11}}A_m + C_m = 0. \tag{18f}$$

$$2aA_0 = \int_{-\infty}^{\infty}\left(\frac{1}{\mu/h} - \frac{1}{\mu^s\xi_s\tan(\xi_s h_s)}\right)\left[(\bar{c}_{44}\xi_0 B_0 + e_{15}C_0)\frac{2\sin^2(qa)}{\pi q^2} + \sum_{m=1}^{\infty}(\bar{c}_{44}\xi_m B_m + e_{15}\alpha_m D_m)\frac{2(-1)^m\sin^2(qa)}{\pi(q^2 - \alpha_m^2)}\right]dq. \tag{18g}$$

$$aA_m = \int_{-\infty}^{\infty}\left(\frac{1}{\mu/h} - \frac{1}{\mu^s\xi_s\tan(\xi_s h_s)}\right)\left[(\bar{c}_{44}\xi_0 B_0 + e_{15}C_0)\frac{2(-1)^m\sin^2(qa)}{\pi(q^2 - \alpha_m^2)} + \sum_{n=1}^{\infty}(\bar{c}_{44}\xi_n B_n + e_{15}\alpha_n D_n)\frac{2(-1)^{m+n}q^2\sin^2(qa)}{\pi(q^2 - \alpha_m^2)(q^2 - \alpha_n^2)}\right]dq. \tag{18h}$$

Eq. (18) contains $2N + 4$ linear algebraic equations with $2N + 4$ undetermined coefficients, in which N stand for the truncation order of the trigonometric series. These coefficients can be numerically obtained by solving the above equations.

In most SHM applications, tone-burst excitations are preferred as they can provide sufficient temporal information for damage diagnoses. The input voltage in time domain can be expressed as

$$V_{in}(t) = \frac{V}{2}\left[1 - \cos\left(\frac{1}{N_C}2\pi f_0 t\right)\right]\sin(2\pi f_0 t), \tag{19}$$

where f_0 is the central frequency, V stands for the voltage amplitude and N_C is the number of cycles. In the present work, five-cycle tone-burst signals are used ($N_C = 5$). Given a certain position x_0, the frequency response function, denoted by $G(\omega)$, can be numerically obtained from Eq. (18). Subjected to an excitation signal $f_e(t)$, the time domain displacement response can be obtained as

$$u(x_0, t) = IF[F(f_e(t)) \cdot G(\omega)], \tag{20}$$

where F() and IF() represent the direct and inverse Fourier transform, respectively.

3. Numerical simulations and improvement of the series

Up to now, a theoretical dynamic model on SH waves that are excited by external voltage imposed on a PZT actuator and propagate along x direction in the plate has been established, for which the closed form expressions of the solution have been obtained. Before investigating its application in SHM, the correctness of the model is first examined. To this end, an aluminum plate with a PZT-5H actuator is considered. For the selected PZT-5H, $c_{44} = 23$GPa, $e_{15} = 17.0$C/m^2, $\varepsilon_{11} = 1.505 \times 10^{-8}$C/Vm, and $\rho^p = 7500$ kg/m^3 [30]. For the aluminum plate, $E = 70$GPa, $v = 0.33$, and $\rho^s = 2700$ kg/m^3. In the present case, only SH0 wave is considered because of its non-dispersive property. The external voltage $V = 1$ V, and the thickness of Al plate is fixed as $h_s = 2$ mm. For the bonding layer, the shear modulus is estimated as 0.468 GPa from the experimental measurements [22] for the 2-component epoxy which will be further used in the experiments of this work. In the calculations, however, this value is rounded to 0.5 GPa throughout the numerical studies. The thickness of the bonding layer usually varies in the range of 1–100 μm [25], depending on the gluing techniques used. Hence, the effect of the thickness h on SH wave generation is worth investigating. Altogether, the effect of the shear modulus μ can be derived directly from the results based on Eq. (6c) (not shown here).

3.1. Convergence of the series

The convergence and the correctness of the series solution are first examined. Tables 1 and 2 respectively show the amplitude of the displacement $|u|$ at a given point of the plate with different truncation orders of the series for the ideal ($h = 0$) and a representative non-ideal ($h = 10$ μm) bonding cases. It can be seen from the tables that the trigonometric series exhibits a good convergence in the frequency range concerned for both cases, irrespective of bonding conditions, structural configurations and receiving positions of the signals. Typically, twenty terms in the series are sufficient to ensure an acceptable accuracy.

3.2. FEM validations

To validate the present model, an FEM model is established using Comsol Multiphysics (with the Partial Differential Equation Module), as shown in Fig. 2. The aluminum plate is set to be long enough in ± x direction, so that for an input tone-burst voltage shown in Eq. (19), SH0 wave will not be reflected within the computed time. In the FEM simulations, the mesh size is set to be smaller than 1/20 of the shortest wavelength and the time step smaller than $1/20f_0$ [6,17]. Besides, re-computations are done using even finer mesh sizes to ensure the convergence and the required accuracy of the numerical results. It can be seen from Fig. 2 that a pure SH0 wave can be excited and captured clearly.

For a typical bonding case with $h = 10$ μm, $2a = 10$ mm, and $h_p = 0.2$ mm, Fig. 3(a) shows the comparison between the theoretical and the FEM results at $x_0 = 20$ mm with the central frequency $f_0 = 150$ kHz. The two curves match very well, in terms of both the temporal, amplitude and phase information. The same consistency can also be observed at different propagating distances and the excitation frequencies, as evidenced in Fig. 3(b)–(d). Besides, SH0 waves with different frequencies in Fig. 3 (a) and (c) show the same arriving time at the same receiving point, which furthermore proves their non-dispersive property. The same phenomenon can also be seen in Fig. 3(b) and (d). Furthermore, FEM validations are also carried out by comparing the frequency tuning curves [25] which are used to characterize the dependence of the wave amplitude on the excitation frequencies, as shown in Fig. 4. In the FEM simulations, the wave amplitudes at each excitation frequency case are extracted with the wavelet transform method [31]. When the external frequency approaches $f_{u\text{-min}}$ in Fig. 4, instead of using the peak amplitude, we simply use the amplitude of the wavelet coefficients at the calculated arriving time of SH0 waves. For example, the amplitude at a receiving point $x_0 = 50$ mm can be extracted from the wavelet coefficients of $t = 0.5/c_{SH0}$. The consistency between the results in both time and frequency domains in these different cases confirms that the proposed

Table 1
Values of $|u|$ at $x_0 = 20$ mm with different truncations of the series for ideal bonding ($h = 0$, $2a = 6$ mm, and $h_p = 0.3$ mm).

$|u|(10^{-9}$m)	$f_0 = 100$ kHz	$f_0 = 200$ kHz	$f_0 = 300$kH	$f_0 = 400$ kHz	$f_0 = 500$kH
$N = 1$	0.081117	0.119097	0.122308	0.082794	0.116833
$N = 2$	0.080946	0.118704	0.122194	0.082723	0.114423
$N = 5$	0.080795	0.118363	0.121979	0.082534	0.110178
$N = 10$	0.080744	0.118234	0.121876	0.082450	0.108409
$N = 20$	0.080730	0.118142	0.121804	0.082409	0.107526

Table 2
Values of $|u|$ at $x_0 = 50$ mm with different truncations of the series for non-ideal bonding ($h = 10$ μm, $2a = 10$ mm, and $h_p = 0.2$ mm).

$|u|(10^{-9}$m)	$f_0 = 50$ kHz	$f_0 = 150$ kHz	$f_0 = 250$kH	$f_0 = 350$ kHz	$f_0 = 450$ kHz
$N = 1$	0.047516	0.085128	0.042566	0.095653	0.164971
$N = 2$	0.047469	0.085056	0.042617	0.095639	0.171180
$N = 5$	0.047410	0.084969	0.042613	0.094511	0.169916
$N = 10$	0.047386	0.084921	0.042594	0.094076	0.169257
$N = 20$	0.047378	0.084804	0.042576	0.093846	0.168939

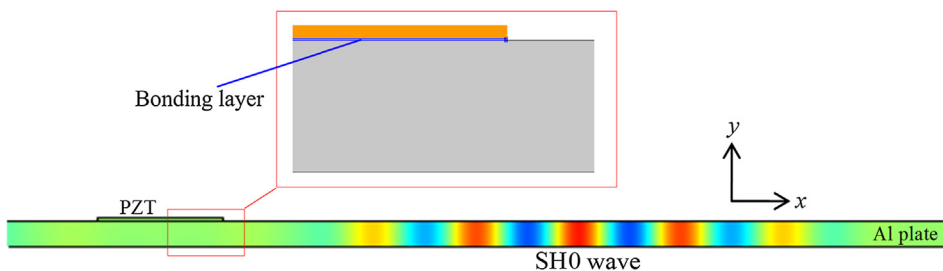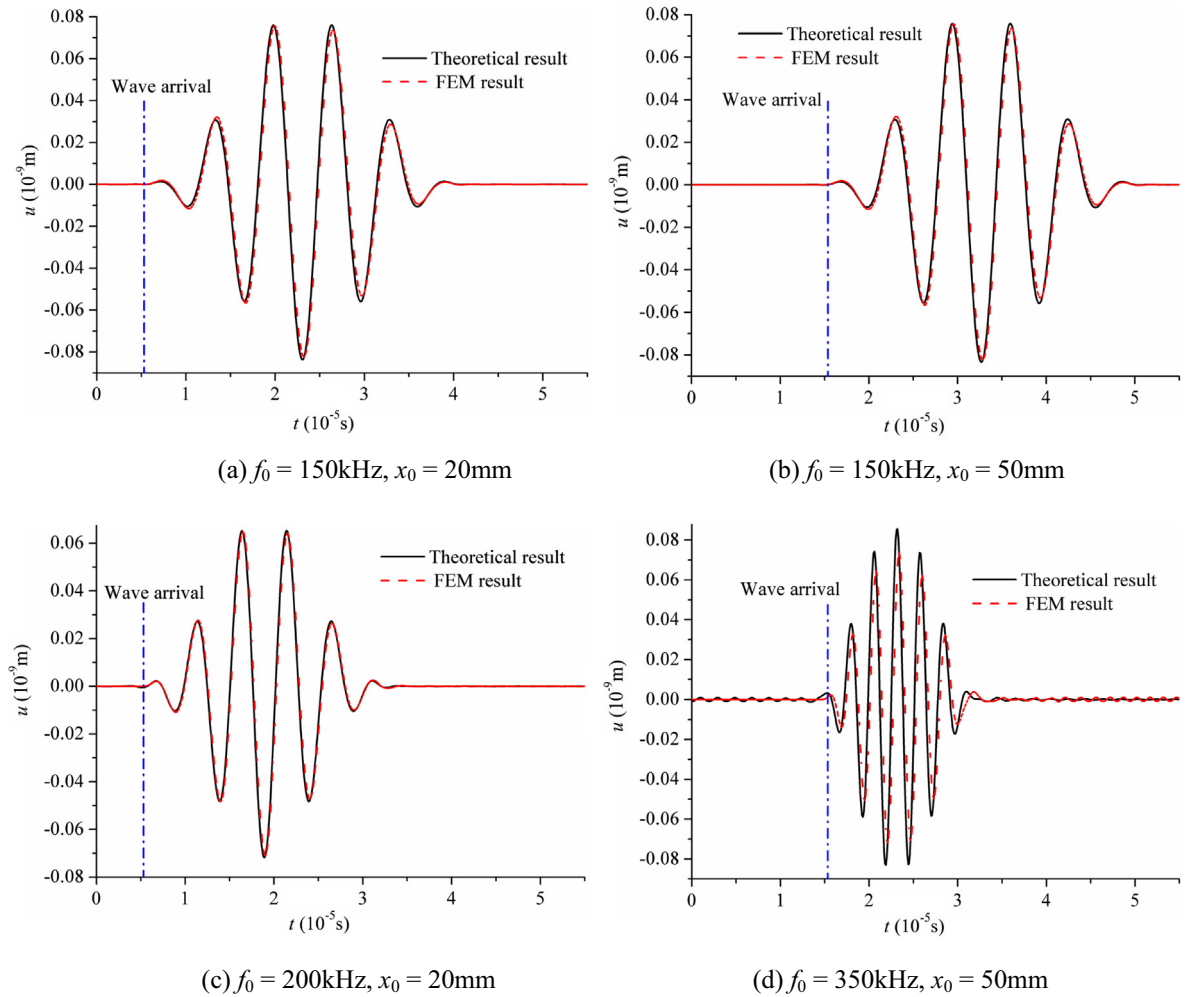**Fig. 2.** FEM model.

Fig. 3. Comparisons between the theoretical and FEM results for the non-ideal bonding case (h = 10 μm, $2a$ = 10 mm, and h_p = 0.2 mm): (a) f_0 = 150 kHz, x_0 = 20 mm; (b) f_0 = 150 kHz, x_0 = 50 mm; (c) f_0 = 200 kHz, x_0 = 20 mm; (d) f_0 = 350 kHz, x_0 = 50 mm.
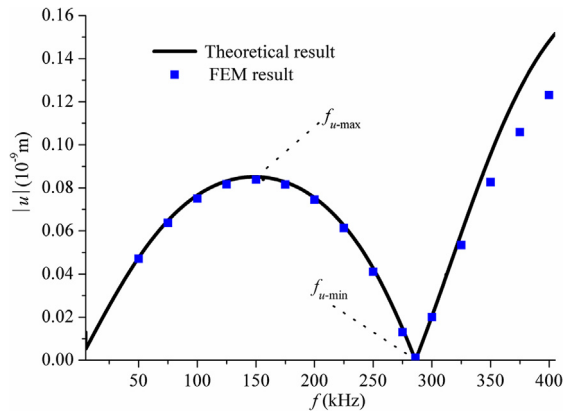

Fig. 4. Comparisons between the frequency tuning curves from the theoretical and FEM results.

theoretical model can be used to accurately predict the generated SH waves. Indeed, when the excitation frequency exceeds $f_{u\text{-min}}$ and starts approaching the resonant frequency (to be discussed later), the amplitude of the response tends to increase significantly, theoretically to infinite but to be bounded to a certain value depending on the system damping. Due to the

highly dynamic nature of the PZT-adhesive-plate assembly in the vicinity of the resonance region, the system response is sensitive to structural details such as damping and other system parameters. This explains the differences observed in this region. For practical SHM applications, however, this is a frequency region that should be avoided. Therefore, the model can meet our need as long as this frequency range, alongside the wave amplitude variation trend, can be correctly predicted.

In addition, we also looked through the results for the ideal bonding case with $h = 0$, $2a = 6$ mm, and $h_p = 0.3$ mm, nice agreement between the theoretical and FEM results in both time and frequency domains can be observed (not shown here). To conclude, the whole set of results demonstrate the validity and the accuracy of the proposed dynamic model, which can be further used to simulate the SH0 wave generation and propagation in a PZT-activated plate and furthermore guide the design of the corresponding SHM systems.

3.3. Truncations of the series

Before the systematic investigations, an improvement or optimization of the algorithm is necessary by establishing a truncation criterion of the series, aiming at truthfully depicting the SH wave generation process while reducing the computational cost at the same time.

Using the realistic bonding case with $h = 10$ μm, Fig. 5(a) shows the comparison between the calculated results with $N = 20$, which has been proved to be convergent and correct, and those with different truncation orders. We can observe that $N = 1$ guarantees very good accuracy for frequencies before the first $f_{u\text{-min}}$. Similarly, for $N = 2$, the result is still convergent before the second $f_{u\text{-min}}$. This trend seems to apply to other cases considered in both Fig. 5(a) and (b), irrespective of the bonding stiffness and PZT dimensions. Considering that the length of PZT approximately equals to the multiple of the wavelength at $f_{u\text{-min}}$, this suggests that the series order to be kept in the calculation should be no less than the non-dimensional ratio $2a/\lambda$ (λ denotes the wavelength). Therefore, a truncation criterion using $N_{cr} = \text{INT}[2a/\lambda] + 1$ is proposed for the trigonometric
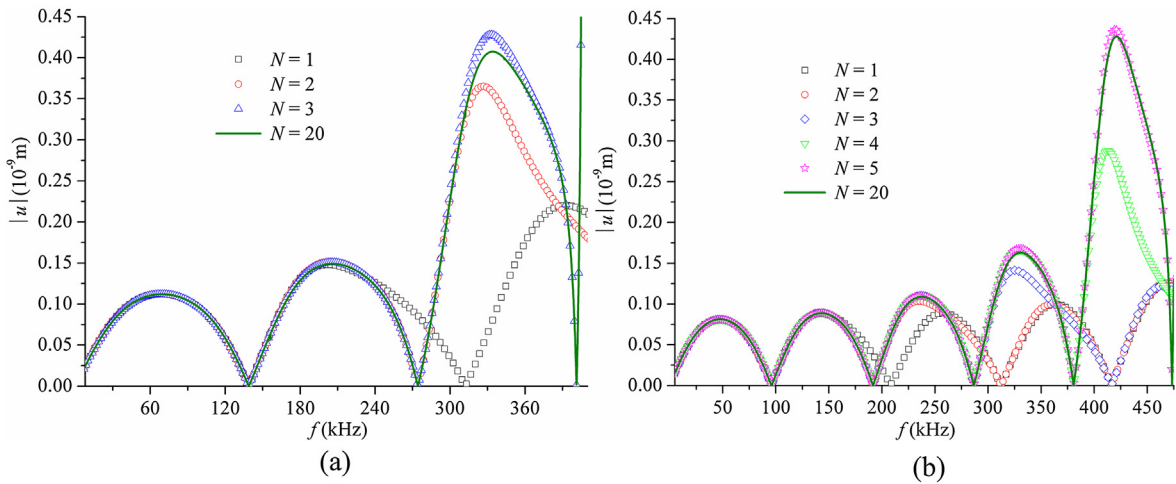
Fig. 5. Excited amplitude of displacement using different truncations: (a) $2a = 20$ mm, $h_p = 0.3$ mm, and $h = 10$ μm; (b) $2a = 30$ mm, $h_p = 0.2$ mm, and $h = 0$.
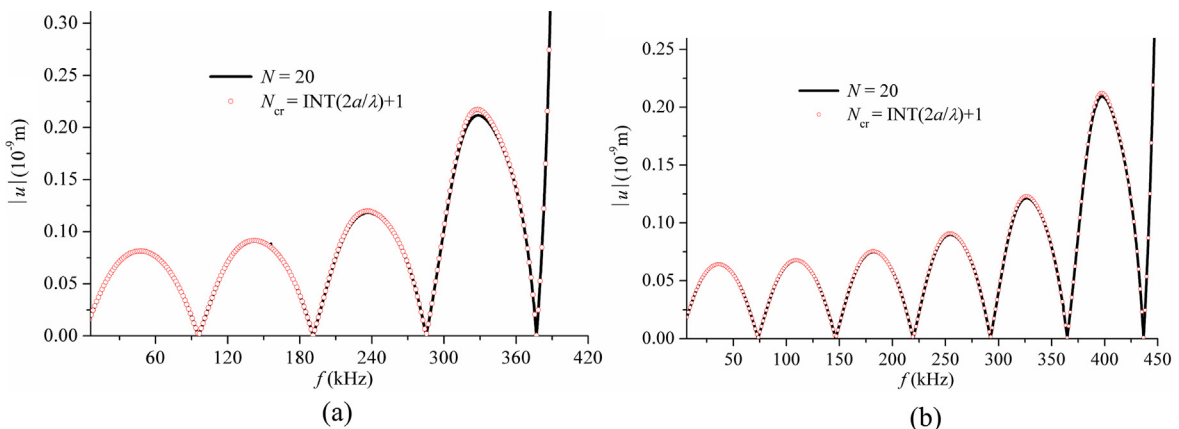
Fig. 6. Verifications of the proposed truncation criterion: (a) $2a = 30$ mm, $h_p = 0.2$ mm, and $h = 10$ μm; (b) $2a = 40$ mm, $h_p = 0.15$ mm, and $h = 0$.

series truncation, in which INT stands for the rounding operation. The displacement amplitude of the SH0 waves calculated using this critical truncation, as well as the reference result using $N = 20$, is shown in Fig. 6, which furthermore proves the correctness of the proposed truncation criterion. This criterion will be adopted in the following simulations and analyses.

4. Experimental validations

Experiments are designed and carried out to further validate the theoretical model and to confirm some important physical phenomena revealed by the model. For the experimental set-up, PZT C6 patches (manufactured by Fuji Ceramics, $c_{44} = 19$GPa, $e_{15} = 14.4$C/m^2, $\varepsilon_{11} = 9.18 \times 10^{-9}$C/Vm, and $\rho^p = 7650$ kg/m^3) of a dimension 10 mm $\times$ 10 mm $\times$ 0.3 mm are
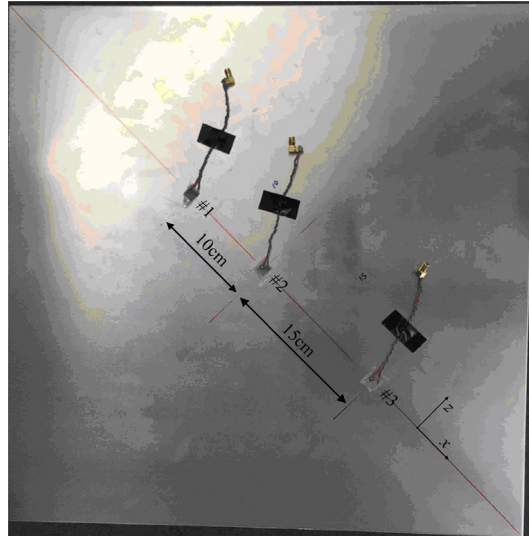

Fig. 7. Layout of the piezoelectric actuator and sensors for SH wave excitation and reception in an aluminum plate.
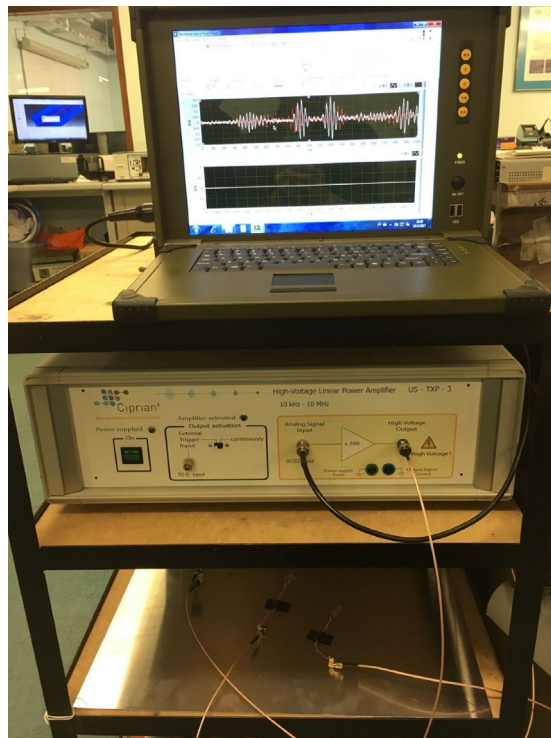

Fig. 8. Measurement system.

bonded on the surface of a 500 mm × 500 mm × 1.6 mm aluminum plate to serve as the transducers. Three SH-PWAS, polarized along positive z direction, are placed along the diagonal direction of an aluminum plate, as shown in Fig. 7. The SH0 wave is first generated by Actuator #1, and received by Sensors #2 and #3, 10 cm and 25 cm away from Actuator #1, respectively. Then the SH-PWAS #2 serves as the actuator and wafer #3 is used for sensing. Experimental process follows the standard test procedure with experimental facilities detailed in [22,31]. A controller commands the NI-PXI5412 signal generation module to output a tone burst excitation signal. The low-voltage signal then passes through a Ciprian US-TXP-3 power amplifier and the amplified output is applied to the piezoelectric transducer to generate SH waves in the plate. Responses of SH waves are then acquired by the NI-PXI5105 data acquisition system, stored and processed by the controller. Fig. 8 shows the photo of the experimental setup used.

Some typical sensor output signals at different central frequencies are shown in Fig. 9 and compared with the theoretical results. As the theoretical model gives the displacement output at a single point and the experiment obtains the voltage output within a finite region, the results are compared in the normalized scale due to the different sensing patterns. It can be seen that the temporal variation and the phase in the theoretical and experimental results match reasonably well. Unwanted S0 mode, inevitably generated by the PZT of finite size, is also detected in experimental signals before the SH0 wave mode, evidenced by the small wave packet in Fig. 9(d). However, due to the difference in the group velocities of S0 and SH0 waves, their corresponding wave packages can be separated in the captured signals. Thus, the generated Lamb wave package was not seen to affect the analyses of the SH0 wave. Besides, some differences between the theoretical and experimental results can be found from the results shown in Fig. 9, which mainly due to the sensing pattern during the experimental process. More specifically, the theoretical result is calculated at a fixed position, for example, $x_0 = 10$ cm in Fig. 10. However, the sensor used in the experiments has a length of 10 mm in the wave propagation direction. The received output signal actually corresponds to the region 9.5 cm $\leq x_0 \leq$ 10.5 cm. This also leads to discrepancies between the theoretical and experimental results.
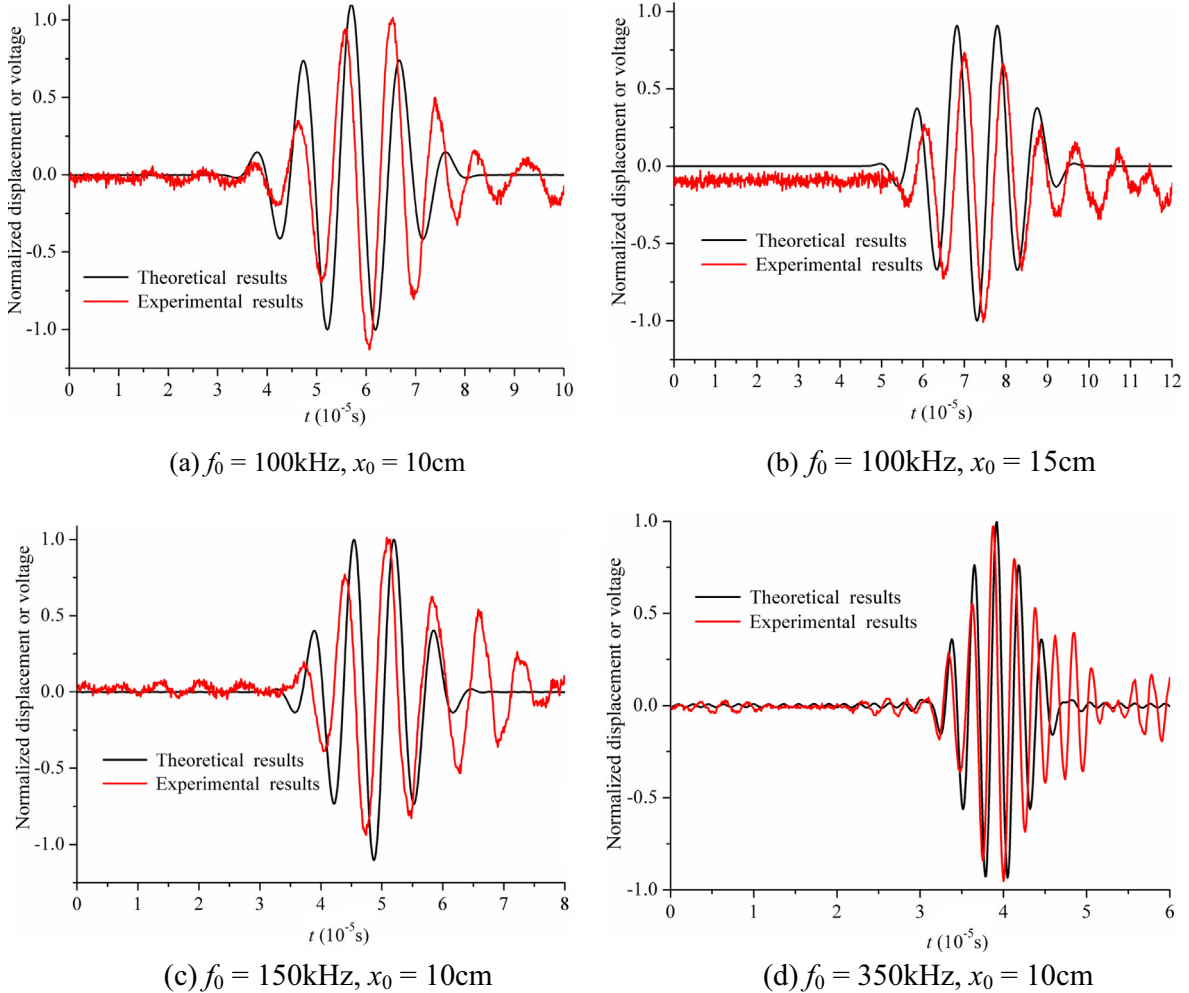

Fig. 9. Comparisons between the theoretical and experimental results: (a) $f_0 = 100$ kHz, $x_0 = 10$ cm; (b) $f_0 = 100$ kHz, $x_0 = 15$ cm; (c) $f_0 = 150$ kHz, $x_0 = 10$ cm; (d) $f_0 = 350$ kHz, $x_0 = 10$ cm.
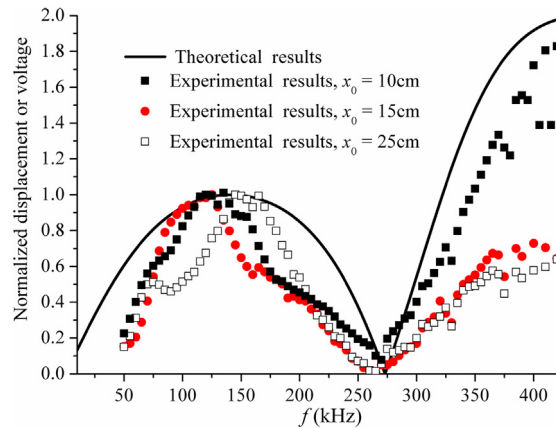
Fig. 10. Comparisons of the frequency tuning curves between theoretical and experimental results.

Although the amplitude information in the theoretical and experimental results cannot be directly compared, their frequency tuning curves can be compared to further validate the theoretical model in the perspective of wave amplitude prediction. To obtain the frequency tuning curves in the experiment, the amplitude of each response signal is extracted with the continuous wavelet transform. Similar to the FEM validation, when the central frequency approaches $f_{u\text{-min}}$, the amplitude of the wavelet coefficients at the wave arrival time is used instead of the peak amplitudes. Finally, the frequency tuning curves in terms of the normalized sensor output voltages of the three aforementioned cases with different wave propagating distances are obtained and compared with the theoretical results, as shown in Fig. 10. The frequency tuning curves from experimental results for different cases have the same tendency with the theoretical prediction, including the locations of $f_{u\text{-max}}$ and $f_{u\text{-min}}$, despite some discrepancies in the amplitude values. In the extremely low frequency region, near-field effect may contribute to these discrepancies between the theoretical and experimental results. However, with the increase of the excitation frequency, especially when the excitation frequency exceeds $f_{u\text{-min}}$, the system will tend to resonate. The responses near the resonant frequency will be very sensitive to the structural details such as material damping and bonding parameters and so forth. It is the complex dynamic behaviors that cause the relatively large discrepancies between the theoretical and experimental results in this frequency region. Besides, as mentioned above, the different sensing patterns between the theoretical and experimental results also contribute to the discrepancies observed in Fig. 10. Nevertheless, although there are some discrepancies between the theoretical and experimental results due to the complex dynamic behaviors of the system when the excitation frequency approaches the resonant frequency, this frequency region should be avoided for SHM applications and therefore this region appears less important to us. All important SHM promising characteristics, such as the frequencies to generate the maximum and minimum wave amplitude, and the general variation of the frequency tuning curves predicted by the theoretical model, are confirmed by experimental results, which implies that the theoretical model can provide all the necessary temporal, phase and amplitude information to guide the SHM design.

5. Discussions

So far, the proposed theoretical model has been validated in both numerical and experimental perspectives. In this section, based on the model, the influence of the dynamic coupling between the PZT and the plate under different bonding conditions is investigated in detail for guiding the design of SH0-wave-based SHM systems. As illustrated in Fig. 4, the generated SH wave amplitude varies with the PZT size as well as the excitation frequencies. Generally speaking, with the increasing excitation frequency, the generated amplitude $|u|$ firstly increases, peaks at $f_{u\text{-max}}$, decreases to a valley at $f_{u\text{-min}}$ before rising up again rapidly. In the present case, the exact peak position is determined to have $2a/\lambda = 0.477$, slightly lower than the commonly accepted rule of thumb of 0.5 when the PZT is considered as an ideal non-dynamic element [15]. At higher frequencies, the system starts to enter into a highly dynamic region in which system resonances are expected. These observations suggest that SH wave generation can be affected by the PZT dynamics and its coupling with the plate, which may pose challenges for further system design. Therefore, a systematic investigation is carried out in three typical frequency regions of the frequency tuning curves in the following sections using a typical benchmark problem ($h_s = 2$ mm and $h^p = 0.3$ mm).

5.1. Peak region and peak positions

The thickness of the bonding layer can certainly affect the amplitude of the generated waves. However, in practical applications, the thickness of the bonding layer is usually hard to be controlled precisely. Therefore, a more feasible scenario would be to choose the optimal excitation frequency for a given thickness of the existing bonding layer, in the peak region and peak positions on the frequency tuning curves. Governed by the inherent PZT length-wavelength relations, the peak

positions are mainly determined by the PZT lengths, as shown in Fig. 11. Taking the particular bonding case ($h = 0$) with a PZT length $2a$ = 8 mm as an example, the maximum SH0 wave amplitude is achieved at f = 181 kHz, which can be considered as the optimal frequency $f_{u\text{-max}}$. When $2a$ = 12 mm, two peaks appear at f = 115 kHz and f = 343.5 kHz, with corresponding $2a/\lambda$ values of 0.443 and 1.32, respectively, smaller than 0.5 and 1.5, the subconscious values in our mind. Although different in values, these observations are consistent with the ones made using Fig. 4. Apart from the PZT length, the dynamic coupling may also affect the peak positions. The coupling strength can be adjusted through changing the bonding conditions. To ascertain this, the $f_{u\text{-max}}$ peak positions are plotted against the bonding stiffness for different PZT lengths in Fig. 12 for both the first and the second peak positions. It can be seen when the PZT length is small, the influence of the bonding conditions is very significant, as evidenced by the steep curves in the figure. Besides, the $f_{u\text{-max}}$ peak positions remain relatively stable when the bonding layer is thin, especially for a large PZT size. Therefore, for a given PZT size and bonding layer thickness, the optimal excitation frequency can be determined using Fig. 12. This finding can be further used to guide the design of the SHM systems in two aspects:

1) If the length of the PZT can be tuned, long PZTs are preferred to ensure a more stable system performance against the variation of the bonding conditions.
2) For a small-sized PZT, precautions should be taken to carefully check the bonding quality in order to ensure an effective wave generation using the right excitation frequency.

5.2. Highly dynamic region and resonance frequencies

Another frequency region of interest is around the resonance frequencies of the system where the system is highly dynamic. Fig. 13 shows the time domain responses (Fig. 13a) of the system under a five-cycle tone-burst excitation with a central frequency of 420 kHz, as well as their corresponding spectra (Fig. 13b) with two different bonding conditions. It can be seen that, when $h = 0$, the excitation frequency is distant from the resonance frequency of the system at 618.5 kHz. Therefore, the generated wave undergoes little distortion. However, when $h = 10$ μm, the system resonance frequency (546.8 kHz) reduces to get closer to the excitation frequency. As a result, the generated SH0 waves are severely distorted and dispersed in frequency as shown in Fig. 13. This divergent signal can hardly be used in SHM applications so that the situation should be avoided. The resonant frequencies of the system for a given configuration and bonding condition can be predicted using the proposed dynamic model.

It is relevant to further quantify the influence of the dynamic coupling through the bonding conditions. Using the same example, the first resonance frequency of the system is calculated and plotted against the thickness of the bonding layer with different PZT lengths in Fig. 14. As expected, a weaker bonding case with a samller h value reduces the resonance frequency, as shown by the downward trend of the curves. Meanwhile, a plate with a longer PZT results in a lower resonance frequency, due to the fact that the equivalent shear modulus $\bar{c}_{44}$ of the PZT is smaller than the shear modulus μ^s of the metal plate. When this happens, the resonance region moves to lower frequencies, thus narrowing down the useful frequency range for SHM. Another observation is that the resonant frequency is quasi-linear with respect to the thickness of the bonding layer in logarithmic scale, which provides a simple way for the systematic assessment. To some extent, it is always preferred to enhance the bonding conditions to achieve a wider low-frequency range for SHM applications.

5.3. Wave distortion around the valley

Having discussed the peak position region (to be used in SHM) and the resonance region (to be avoided in SHM), a closer look is taken at the valley region surrounding $f_{u\text{-min}}$ on the frequency tuning curve to complete the coupling analyses. By
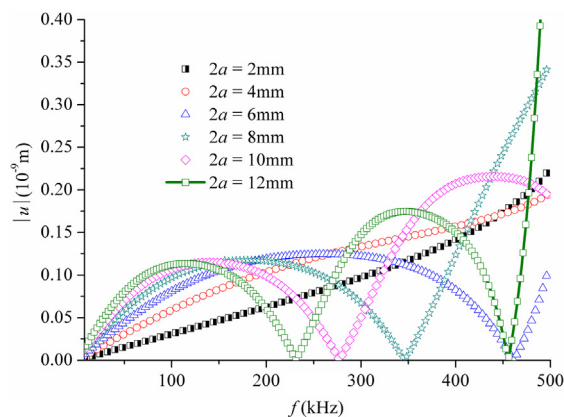

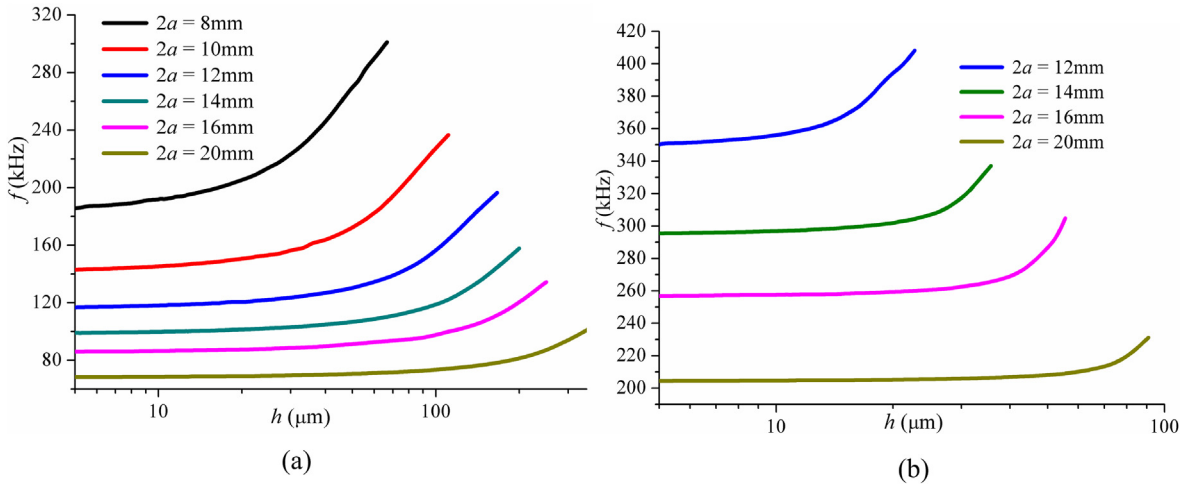**Fig. 11.** Excited displacement amplitude for different PZT lengths ($h = 0$).

Fig. 12. Relationship between the first two $f_{u\text{-max}}$ peak positions and the bonding layer thickness h: (a) the first peak position; (b) the second peak position.

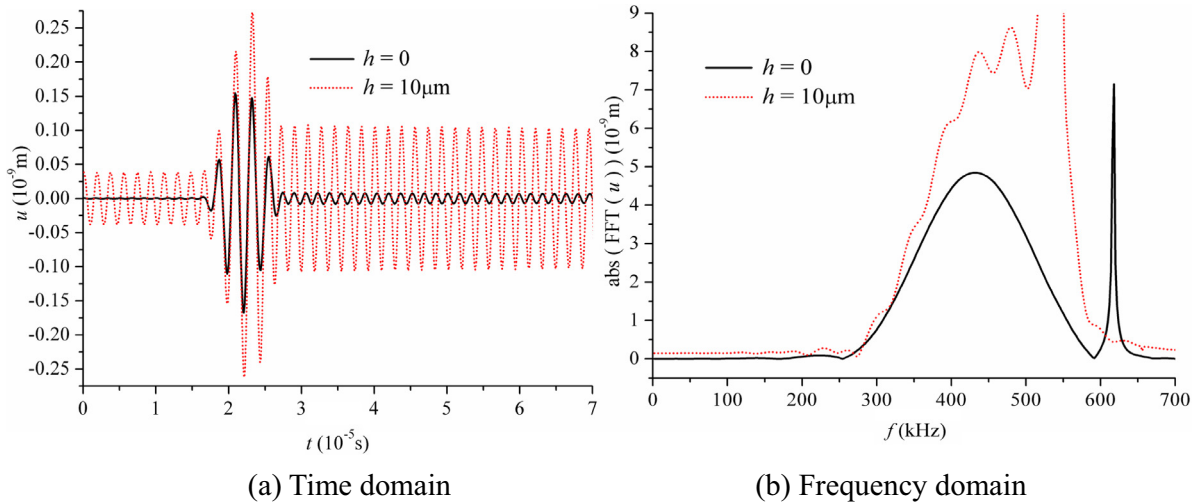(a) Time domain   (b) Frequency domain

Fig. 13. Displacement responses in the time domain (a) and the corresponding amplitude spectrums in the frequency domain (b) ($x_0 = 50$ mm, $f_0 = 420$ kHz, and $2a = 4$ mm).
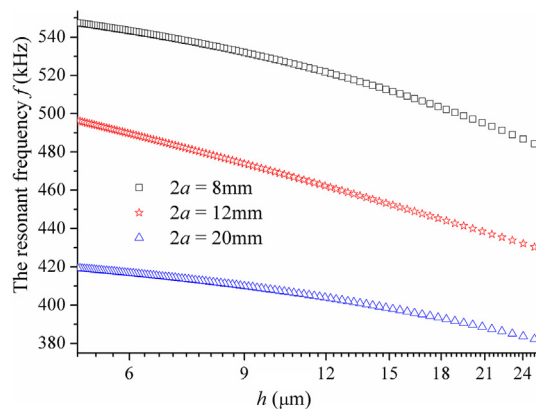

Fig. 14. Variations of the first resonance frequency with respect to the thickness of bonding layer.

varying the central frequency of the excitation f_0 around $f_{u\text{-min}}$, calculations using the proposed model and the FEM both reveal a split of the generated SH0 wave packet to various extents, as shown in Fig. 15. A plausible explanation can be made as follows. According to the frequency tuning curve shown in Fig. 4, wave generation at $f_{u\text{-min}}$ is minimal. Since the excitation

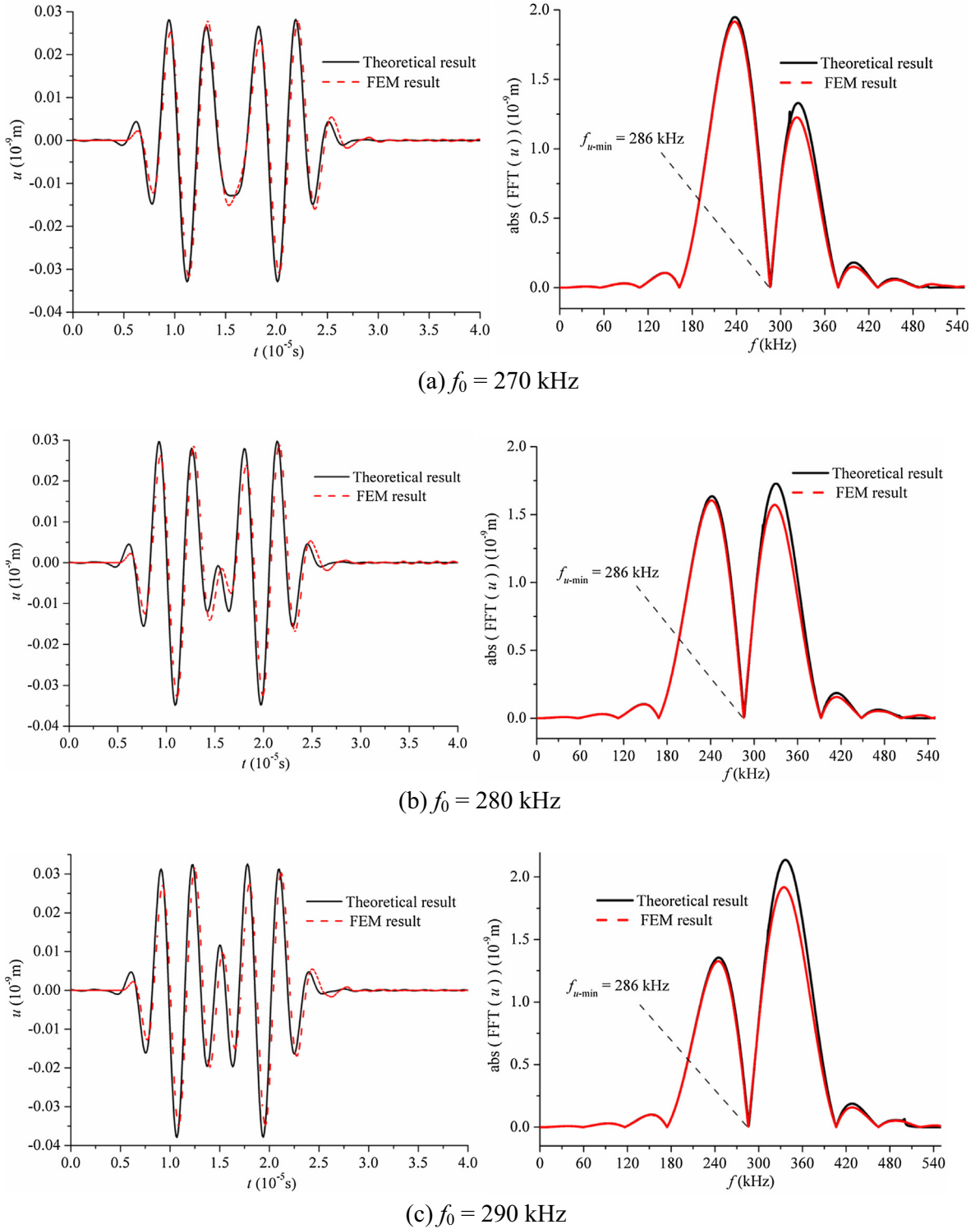(a) f_0 = 270 kHz

(b) f_0 = 280 kHz

(c) f_0 = 290 kHz

Fig. 15. Wave distortion phenomenon observed during theoretical and numerical analyses (the PZT 5H-Aluminum composites with $2a$ = 10 mm, h_p = 0.2 mm and h_s = 2.0 mm): (a) f_0 = 270 kHz; (b) f_0 = 280 kHz; (c) 290 kHz. The left and right figures are respectively the displacement responses in time domain and the corresponding amplitude spectra in frequency domain.
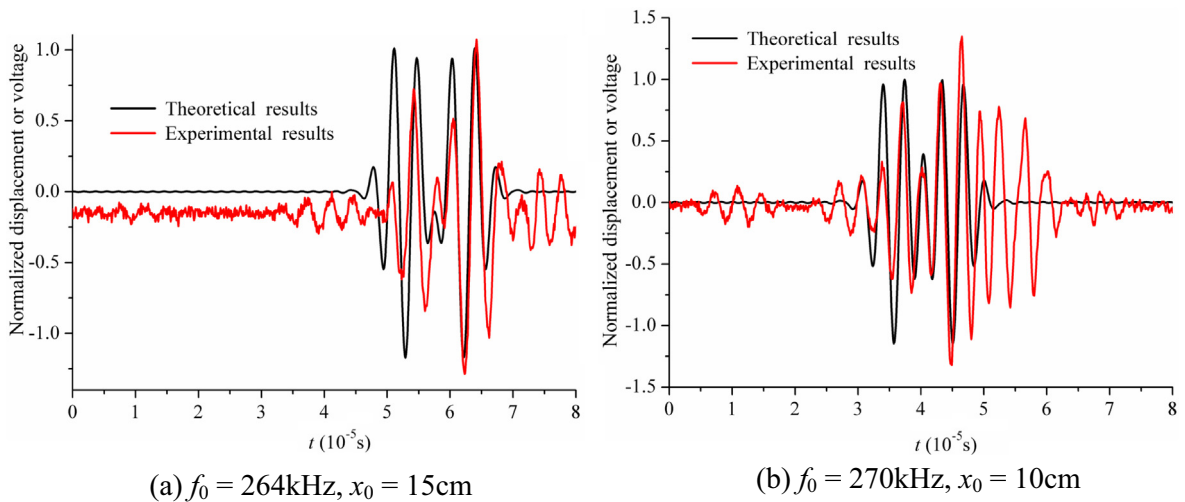
Fig. 16. Wave distortion observed in experiments (PZT C6-Aluminum composites with $2a = 10$ mm, $h_p = 0.3$ mm and $h_s = 1.6$ mm): (a) $f_0 = 264$ kHz, $x_0 = 15$ cm; (b) $f_0 = 270$ kHz, $x_0 = 10$ cm.

(a) $f_0 = 264$kHz, $x_0 = 15$cm   (b) $f_0 = 270$kHz, $x_0 = 10$cm

signal has a certain frequency band near the central frequency, the side band responses dominate to create such a phenomenon, as evidenced by the transformed amplitude spectrums (FFT results) shown in Fig. 15. Due to the finite PZT patch adopted during experimental process, unwanted S0 mode waves can be clearly seen before SH0 waves in Fig. 16. Meanwhile, the wave distortion phenomenon is also confirmed by experiments, as shown in Fig. 16. The shape of the two split waves is dependent on many factors, such as the initial excitation signal, external frequency, $f_{u\text{-min}}$, and the slope of the frequency turning curve near $f_{u\text{-min}}$. Therefore, the two split wave packages are not necessarily to be even theoretically. In addition, when the excitation frequency approaches $f_{u\text{-min}}$, the generated SH wave amplitude will be very small. In this case, other factors which would be neglected under the normal SH wave dominance can no longer be overlooked and start to show effects. Therefore, the revelation of the phenomenon and its experimental confirmation demonstrate again the capability of the proposed model in depicting the fine details of the physical phenomena.

This situation should, again, be avoided in practical SHM exercises. Should this happen, the splitted waves might be misunderstood as two separate wave packets. Moreover, the extracted amplitude information may be easily overwhelmed by the wave components of the side bands. This may further mislead the damage diagnosis.

6. Conclusions

A theoretical model for the SH0 wave generation is established in this study, in which the full dynamics of the PZT actuators are considered and coupled to a plate through an elastic bonding layer, through the consideration of its thickness and shear modulus. Analytical solutions, which can simultaneously satisfy the governing dynamic equations and boundary conditions, are obtained in a closed form using trigonometric series and modal superposition method. The fast convergence of the series solutions and their good accuracy are demonstrated with the aid of FEM results in both time and frequency domains. To maximize the calculation efficiency, a truncation criterion for the series selection is proposed, based on the size of the PZT actuators and the wavelength of SH0 waves. Additionally, experiments are also carried out to further validate the theoretical results. Finally, systematic analyses on the dynamic coupling and the SH wave generation are carried out from SHM perspectives.

Results predicted by the proposed model agree well with both FEM and experimental results in terms of the temporal, phase and amplitude of the generated SH0 waves, in a wide frequency range before approaching the system resonance. Closer to the system resonance, the accuracy of the model deteriorates in terms of wave amplitude prediction due to the increasing sensitivity of the system response to structural details. Fortunately, this is a frequency range that should be avoided in SHM applications. Numerical analyses show the influence of the dynamic coupling on the SH0 wave generation in terms of both peak, valley and the resonance region of the frequency tuning curves. The prevailing conclusion of the analyses is that the PZT-adhesive-plate forms a coupled dynamic system, whose dynamic coupling impacts on the SH0 wave generation, and consequently on the SHM applications. More specifically, it is shown that, due to the dynamic coupling, the optimal excitation frequency differs from (lower than) the common rule of thumb of $2a/\lambda = 0.5, 1.5, \ldots\ldots$. The determination of the accurate values, however, would need a comprehensive analysis and calculation using a fully-coupled dynamic model like the present one. When reaching the valley of the frequency tuning curve, the generated waves are split into two wave packets dominated by the energy of the sidebands. Finally, at even higher frequencies approaching the resonance frequencies of the system, severe signal distortions take place due to the strong system dynamics. These last two scenarios should be and can be avoided in the design of practical SHM system through simulations using the proposed model.

It is relevant to summarize the major contribution of the work form SHM perspective. The proposed model, by virtue of its fully coupled nature, is different from existing ones and provides a new analysis tool on a PZT-adhesive-plate system. In physical perspective, the model allows the prediction of the system resonances as well as the evaluation of the effect of the adhesive layers. Numerical analysis demonstrates the implication of this coupling in terms of wave generation when approaching the highly dynamic region of the system. Finally, the model shows its ability to enable efficient and systematic evaluation of the effects of various system parameters on the practical design of an SHM system, such as the excitation frequency, bonding thickness of the adhesive, and the size of PZT.

As a final remark, the present model presents a unified platform for physical mechanism exploration, structural design and eventually system optimization for SH0 wave based SHM applications. As a side issue, the Lamb mode generation, such as the unwanted affiliated S0 mode caused by the finite PZT pitch, is a useful and interesting topic. Its generation, as well as its mutual effect with SH0 waves, deserves a separate and systematic investigation in further work.

Acknowledgment

References

[1] C.B. Xu, Z.B. Yang, X.F. Chen, S.H. Tian, Y. Xie, Circular sensing networks for guided waves based structural health monitoring, Mech. Syst. Signal Process. 66–67 (2016) 248–267.
[2] L. Wang, F.G. Yuan, Damage identification in a composite plate using prestack reverse-time migration technique, Struct. Health Monit. 4 (2005) 195–211.
[3] M. Mańka, M. Rosiek, A. Martowicz, T. Stepinski, T. Uhl, PZT based tunable interdigital transducer for lamb waves based NDT and SHM, Mech. Syst. Signal Process. 78 (2016) 71–83.
[4] J. Jia, Q. Wang, Z. Liao, Y. Tu, S.-T. Tu, Design of waveguide bars for transmitting a pure shear horizontal wave to monitor high temperature components, Materials 10 (2017) 1027.
[5] H.S. Yoon, D. Jung, J.H. Kim, Lamb wave generation and detection using piezoceramic stack transducers for structural health monitoring applications, Smart Mater. Struct. 21 (2012) 055019.
[6] J. Pohl, C. Willberg, U. Gabbert, G. Mook, Experimental and theoretical analysis of Lamb wave generation by piezoceramic actuators for structural health monitoring, Exp. Mech. 52 (2012) 429–438.
[7] W. Zhou, H. Li, F.G. Yuan, Fundamental understanding of wave generation and reception using d_{36} type piezoelectric transducers, Ultrasonics 57 (2015) 135–143.
[8] A. Kamal, V. Giurgiutiu, Shear horizontal wave excitation and reception with shear horizontal piezoelectric wafer active sensor (SH-PWAS), Smart Mater. Struct. 23 (2014) 085019.
[9] P. Belanger, G. Boivin, Development of a low frequency omnidirectional piezoelectric shear horizontal wave transducer, Smart Mater. Struct. 25 (2016) 045024.
[10] Y.Y. Kim, Y.E. Kwon, Review of magnetostrictive patch transducers and applications in ultrasonic nondestructive testing of waveguides, Ultrasonics 62 (2015) 3–19.
[11] J.S. Lee, Y.Y. Kim, S.H. Cho, Beam-focused shear-horizontal wave generation in a plate by a circular magnetostrictive patch transducer employing a planar solenoid array, Smart Mater. Struct. 18 (2009) 015009.
[12] Q. Wang, S.T. Quek, V.K. Varadan, Analytical solution for shear horizontal wave propagation in piezoelectric coupled media by interdigital transducer, J. Appl. Mech.-T. ASME 72 (2005) 341–350.
[13] P.D. Wilcox, P. Cawley, M.J.S. Lowe, Acoustic fields from PVDF interdigital transducers, IEE P.- Sci Meas. Tech. 145 (1998) 250–259.
[14] A.V. Harish, P. Ray, P. Rajagopal, K. Balasubramaniam, B. Srinivasan, Detection of fundamental shear horizontal mode in plates using fibre Bragg gratings, J. Intell. Mater. Syst. Struct. 27 (2016) 2229–2236.
[15] H. Miao, Q. Huan, Q. Wang, F. Li, A new omnidirectional shear horizontal wave transducer using face shear (d_{24}) piezoelectric ring array, Ultrasonics 74 (2017) 167–173.
[16] H. Miao, Q. Huan, F. Li, Excitation and reception of pure shear horizontal waves by using face-shear d_{24} mode piezoelectric wafers, Smart Mater. Struct. 25 (2016) 11LT01.
[17] H. Miao, S. Dong, F. Li, Excitation of fundamental shear horizontal wave by using face-shear (d_{36}) piezoelectric ceramics, J. Appl. Phys. 119 (2016) 174101.
[18] W. Zhou, H. Li, F.G. Yuan, Guided wave generation, sensing and damage detection using in-plane shear piezoelectric wafers, Smart Mater. Struct. 23 (2014) 015014.
[19] P.S. Lowe, T. Scholehwar, J. Yau, J. Kanfoud, T.-H. Gan, C. Selcuk, Flexible shear mode transducer for structural health monitoring using ultrasonic guided waves, IEEE Trans. Ind. Inform. (2017), https://doi.org/10.1109/TII.2017.2775343.
[20] K.A. Tiwari, R. Raisutis, L. Mazeika, V. Samaitis, 2D analytical model for the directivity prediction of ultrasonic contact type transducers in the generation of guided waves, Sensors 18 (2018) 987.
[21] Q. Huan, H. Miao, F. Li, Generation and reception of shear horizontal waves using the synthetic face-shear mode of a thickness-poled piezoelectric wafer, Ultrasonics 86 (2018) 20–27.
[22] S. Shan, L. Cheng, P. Li, Adhesive nonlinearity in Lamb-wave-based structural health monitoring systems, Smart Mater. Struct. 26 (2017) 025019.
[23] W.Q. Chen, K.Y. Lee, Exact solution of angle-ply piezoelectric laminates in cylindrical bending with interfacial imperfections, Compos. Struct. 65 (2004) 329–337.
[24] N. Mori, S. Biwa, T. Hayashi, Reflection and transmission of Lamb waves at an imperfect joint of plates, J. Appl. Phys. 113 (2013) 074901.
[25] V. Giurgiutiu, Tuned Lamb wave excitation and detection with piezoelectric wafer active sensors for structural health monitoring, J. Intell. Mater. Syst. Struct. 16 (2005) 291–305.
[26] P. Li, L. Cheng, Shear horizontal wave propagation in a periodic stubbed plate and its application in rainbow trapping, Ultrasonics 84 (2018) 244–253.
[27] M. Mahinzare, H. Ranjbarpur, M. Ghadiri, Free vibration analysis of a rotary smart two directional functionally graded piezoelectric material in axial symmetry circular nanoplate, Mech. Syst. Signal Process. 100 (2018) 188–207.
[28] J.S. Yang, Z.G. Chen, Y.T. Hu, Vibration of a thickness-twist mode piezoelectric resonator with asymmetric non-uniform electrodes, IEEE Trans. Ultrason. Ferroelectr. Freq. Control 55 (2008) 841–848.

[29] B. Zhang, A. Bostrom, A.J. Niklasson, Antiplane shear waves from a piezoelectric strip actuator: exact versus effective boundary condition solutions, Smart Mater. Struct. 13 (2004) 161–168.
[30] H.Y. Fang, J.S. Yang, Q. Jiang, Rotation-perturbed surface acoustic waves propagating in piezoelectric crystals, Int. J. Solids Struct. 37 (2000) 4933–4947.
[31] S. Shan, L. Cheng, F. Wen, Characterization of nonplanar second harmonic Lamb waves with a refined nonlinear parameter, J. Nondest. Evaluat. Diagnostics Prognost. Eng. Syst. 1 (2018) 011004.